XRISM/Resolve spectroscopy of the central engine in the Seyfert-1 AGN Mrk 279

Miller, J.M.; Xiang, X.; Byun, D.; Behar, E.; Brenneman, L.; Cackett, E.; ... ; Zoghbi, A.

The Astrophysical Journal Letters, 994:L10 (9pp), 2025 November 20 https://doi.org/10.3847/2041-8213/ae1606

XRISM/Resolve Spectroscopy of the Central Engine in the Seyfert-1 AGN Mrk 279

Jon M. Miller[1], Xin Xiang[1], Doyee Byun (변도의)[1], Ehud Behar[2], Laura Brenneman[3], Edward Cackett[4], Elisa Costantini[5,6], Luigi Gallo[7], Keith Horne[8], Elias Kammoun[9], Chen Li[10], and Abderahmen Zoghbi[11,12,13]
[1] Department of Astronomy, University of Michigan, MI 48109, USA; jonmm@umich.edu
[2] Department of Physics, Technion, Technion City, Haifa 3200003, Israel
[3] Center for Astrophysics | Harvard-Smithsonian, MA 02138, USA
[4] Department of Physics and Astronomy, Wayne State University, Detroit, MI 48201, USA
[5] SRON Space Research Organization Netherlands, Niels Bohrweg 4, 2333CA Leiden, The Netherlands
[6] Anton Pannekoek Institute for Astronomy, University of Amsterdam, Science Park 904, NL-1098 XH Amsterdam, The Netherlands
[7] Department of Astronomy and Physics, Saint Mary's University, Nova Scotia B3H 3C3, Canada
[8] SUPA Physics and Astronomy, University of St. Andrews, Fife, KY16 9SS, UK
[9] Cahill Center for Astrophysics, California Institute of Technology, Pasadena, CA 91125, USA
[10] Leiden Observatory, Leiden University, PO Box 9513, 2300 RA Leiden, The Netherlands
[11] Department of Astronomy, The University of Maryland, College Park, MD 20742, USA
[12] HEASARC, Code 6601, NASA/GSFC, Greenbelt, MD 20771, USA
[13] CRESST II, NASA Goddard Space Flight Center, Greenbelt, MD 20771, USA
Received 2025 September 17; revised 2025 October 17; accepted 2025 October 22; published 2025 November 12

Abstract

High-resolution X-ray spectroscopy with XRISM gives an unprecedented view of the "central engine" in active galactic nuclei (AGN), providing unique insights into black hole accretion and feedback. We present an analysis of the first XRISM/Resolve spectrum of the Seyfert-1 galaxy Mrk 279, known for its complex line profiles and variability. The data reveal velocity components within the Fe K_α emission line that can be associated with the inner face of the molecular torus ($r \geqslant 10^4 GM/c^2$), the broad-line region (BLR; $r = 1650^{+5780}_{-1480}\ GM/c^2$), and the inner accretion disk ($r = 81^{+280}_{-75}\ GM/c^2$). We find evidence of low-velocity, highly ionized gas that contributes an H-like Fe XXVI emission line at 6.97 keV, confirming suggestions from prior low-resolution spectra. The data do not show slow winds in absorption, but two pairs of lines—consistent with He-like and H-like Fe shifted by $v \simeq 0.22c$ and $v \simeq 0.33c$—improve the fit and could represent an ultrafast outflow (UFO). Their addition to the model only reduces the Akaike information criterion by 3.6 and 3.5, respectively, signaling modest support. Additional observations are needed to definitively test for the presence of fast X-ray winds in Mrk 279. We discuss these results in the context of the geometry of the central engine in AGN, emerging trends in XRISM studies of AGN, and the nature of the potential UFOs.

Unified Astronomy Thesaurus concepts: X-ray active galactic nuclei (2035); Astrophysical black holes (98); Black hole physics (159); Accretion (14)

1. Introduction

The region between the innermost stable circular orbit (ISCO) and the molecular torus is sometimes referred to as the "central engine" in active galactic nuclei (AGN). It is within this expanse—perhaps $\Delta r \simeq 10^5 GM/c^2$—that accretion generates radiative and mechanical feedback that can reshape host galaxies. Ironically, although interferometry has imaged the shadow of the event horizon and the torus (e.g., Event Horizon Telescope Collaboration et al. 2019, Gravity Collaboration et al. 2024), we are not yet able to directly image the orders of magnitude in between these extremes. Spectroscopy, variability, and other tools must be harnessed to understand this region.

In some key respects, X-rays may be the most incisive probe of the central engine. Unlike the UV and EUV light that dominate the radiative output from AGN, X-rays are not as easily attenuated by gas and dust, X-ray lines are excited by the X-ray continuum captured by the same instrument, and the host galaxy does not contribute much background. With the launch of XRISM, X-ray spectroscopy has taken a major step forward. The Resolve calorimeter delivers a resolution of $\Delta E = 4.5$ eV in the Fe K band, or $R = E/\Delta E \geqslant 1400$ (for descriptions of XRISM and its instruments, see K. Hayashida et al. 2018; M. Tashiro et al. 2021; Y. Ishisaki et al. 2022). It is in this band that the neutral Fe K_α line is found—the best X-ray diagnostic of the distribution of cold gas—as well as the most powerful, highly ionized winds (for a review, see L. C. Gallo et al. 2023).

XRISM spectroscopy of the nearby Seyfert-1.5 galaxy NGC 4151 reveals separate contributions to the Fe K_α line from radii that are broadly consistent with the inner face of the molecular torus, the optical "broad-line region" (BLR), and the disk close to the ISCO (XRISM Collaboration et al. 2024). The same observations reveal a rich wind spectrum, with component velocities in the range of $2 \times 10^2 \leqslant v \leqslant 5 \times 10^4\ \mathrm{km\ s^{-1}}$ (X. Xiang et al. 2025). The kinetic power of the fastest wind components appears to exceed the threshold at 0.5%–5% of the Eddington limit, identified in simulations as the threshold for reshaping host galaxy structure (T. Di Matteo et al. 2005, P. F. Hopkins & M. Elvis 2010).

It is possible that Seyfert-1.5 AGN afford a fortuitous view of the central engine, sampling a large range of radii, geometries, and physical processes, but additional observations of related AGN are needed to confirm this. To this end,

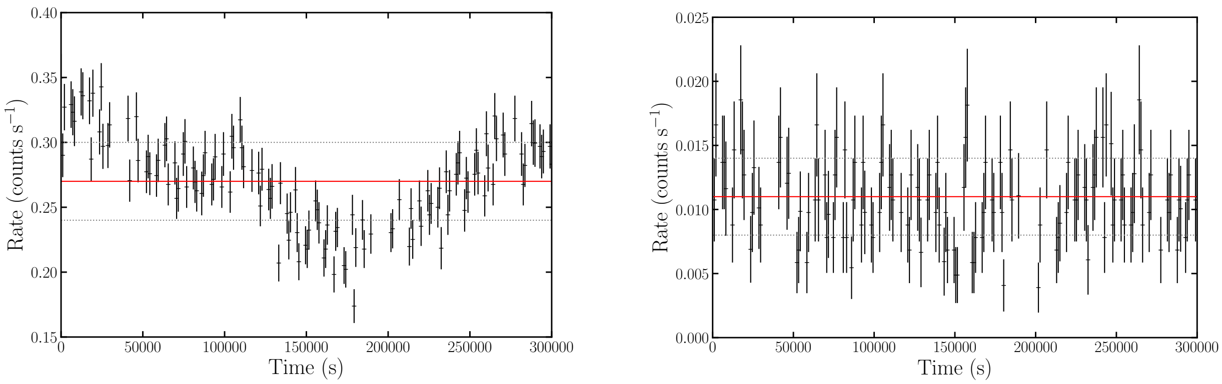

Figure 1. Light curves of the XRISM/Resolve observation of Mrk 279. The left panel shows the light curve of the full Resolve band, and the right panel shows the light curve of the filtered 6.3–6.5 keV band (6.1–6.3 keV in the observed frame). The red horizontal line in each panel indicates the mean rate in each band (0.27 ± 0.03 counts s^{-1} for the full band, 0.011 ± 0.003 counts s^{-1} for 6.1–6.3 keV), and the horizontal dotted lines indicate the rms of the variations in each curve.

we observed the Seyfert-1 galaxy Mrk 279 ($z = 0.0305$; M. A. Strauss & J. Huchra 1988) during XRISM Cycle 1. At $M_{\rm BH} = 3.8^{+0.9}_{-0.6} \times 10^7\, M_\odot$ (P. R. Williams et al. 2018), the mass of the black hole in Mrk 279 is similar to that in NGC 4151 ($M_{\rm BH} = 3.4 \pm 0.4 \times 10^7\, M_\odot$; M. C. Bentz & S. Katz 2015), but its Eddington fraction is potentially 1 order of magnitude higher (R. V. Vasudevan & A. C. Fabian 2007). Importantly, prior observations with XMM-Newton suggest a composite Fe K_α emission line in Mrk 279 (E. Costantini et al. 2010), and Chandra spectra reveal broadened He-like O VII lines that likely originate in the BLR (E. Costantini et al. 2007).

In this Letter, we report on the first XRISM observation of Mrk 279. Section 2 describes the key observation details and how the data were reduced. Our analysis procedure and results are described in Section 3. Finally, in Section 4, we discuss our results and their impact on our understanding of Mrk 279 specifically and AGN central engines in general.

2. Observation and Data Reduction

XRISM observed Mrk 279 starting on 2024 September 19, starting at 19:58:04 UTC. The high-resolution Resolve calorimeter (Y. Ishisaki et al. 2022) was run in its standard "PX_NORMAL" mode. The Xtend CCD camera (K. Hayashida et al. 2018) was run in the "Window1" mode to limit photon pileup in the data. Prior studies with XMM-Newton have observed Mrk 279 at CCD resolution (e.g., E. Costantini et al. 2010), so this work is focused on the Resolve spectrum.

When XRISM observed Mrk 279, the gate valve was in a closed position, truncating the spectrum below 1.6 keV and reducing the total effective area across the passband. The data were reduced following the XRISM Quick-Start Guide v2.3, via HEASOFT version 6.34 and the associated calibration files and tools. Briefly, the data were filtered to exclude anomalies in low-Earth orbit, and events from the calibration pixel (36) and pixels 11 and 27 were excluded. The data were further screened to include only high-resolution primary events, which have a resolution of approximately 4.5 eV (XRISM Collaboration et al. 2024). The light curve of the full Resolve band shows only modest variability (see Figure 1, left panel), while the light curve of the Fe K band is entirely consistent with a constant count rate (see Figure 1, right panel). The resulting spectrum is constructed with default bins of 0.5 eV, and the tools `rslmkrmf` and `xaarfgen` are used to make the redistribution matrix file (rmf) and ancillary response file. We elected to create a "Large" rmf. After all screening, the net Resolve exposure time was 168 ks.

NuSTAR and XMM-Newton made contemporaneous observations of Mrk 279 in support of this XRISM effort. A joint analysis of the data from all three observatories will be presented in a forthcoming paper (D. Byun et al. 2025, in preparation).

3. Reduction and Analysis

All spectral modeling was done using SPEX version 3.08.01 (J. S. Kaastra et al. 1996), minimizing a Cash statistic (W. Cash 1979). Within SPEX, the data were binned prior to fitting, using the "optimal" binning algorithm of J. S. Kaastra & J. A. M. Bleeker (2016). To boost the sensitivity of the data, the data were further binned by a uniform factor of 4.0. The XRISM/Resolve spectrum was fit over the 2.0–12.0 keV band to avoid calibration uncertainties at low energy and to avoid background effects at high energy.

Following XRISM Collaboration et al. (2024) we adopted a model with a blackbody peaking in the UV and an attenuated power-law continuum in the X-ray band. XRISM observations of the Seyfert-1 galaxies NGC 4151 and NGC 3783 both require multiple velocity components to describe the Fe K_α emission lines observed in these systems (XRISM Collaboration et al. 2024, M. Mehdipour et al. 2025); accordingly, we allowed for up to three velocity components. Finally, we searched for photoionized absorption and emission components, following the detection of a broad range of outflows in NGC 4151 (X. Xiang et al. 2025) and NGC 3783 (M. Mehdipour et al. 2025) and extremely fast flows in PDS 456 (XRISM Collaboration et al. 2025).

3.1. Basic Emission Model

To provide a relatively model-independent characterization of the Fe K_α line complex in Mrk 279, we first consider only a basic model with an attenuated power-law X-ray continuum and emission-line components. We use the "pow" component within SPEX, plus two "etau" components to bend the function to zero flux at low and high energy. Although many variations on a broken power law are possible via "pow," only a single power-law index, Γ, and flux normalization are allowed to vary. At calorimeter resolution, the two components of the Fe K_α line become evident, and a simple line core is inadequate. To account for this atomic structure, we use the "mytorus" line

Table 1
Basic Model Parameters

Component	Parameter	Value
Power Law	Γ	$1.68^{+0.01}_{-0.01}$
	$A(10^{44}$ ph s^{-1} keV$^{-1})$	$1.06^{+0.02}_{-0.02} \times 10^{8}$
MYTorus #1	Normalization	$9.2^{+2.5}_{-2.5} \times 10^{7}$
	σ_v (km s^{-1})	370^{+150}_{-170}
MYTorus #2	Normalization	$1.5^{+0.3}_{-0.3} \times 10^{8}$
	σ_v (km s^{-1})	2200^{+600}_{-500}
MYTorus #3	Normalization	$2.2^{+0.6}_{-0.6} \times 10^{8}$
	σ_v (km s^{-1})	$20^{+6}_{-4} \times 10^{3}$
	C-Statistic	729.5
	dof	679

Note. Parameters of the best-fitting basic model of the XRISM/Resolve spectrum of Mrk 279, assuming a power-law continuum and three Gaussian convolved `MYTorus` components. The models were fit to the time-averaged XRISM spectrum. With this model, the observed flux is $F_{2-10} = 2.1 \times 10^{-11}$ erg cm^{-2} s^{-1}, implying a luminosity of $L_{\rm ion}^{\rm all} = 1.3 \times 10^{45}$ erg s^{-1}.

model (K. D. Murphy & T. Yaqoob 2009). This model has been employed to fit Resolve spectra from NGC 4151, Cen A, and M81* (XRISM Collaboration et al. 2024; D. Bogensberger et al. 2025; J. M. Miller et al. 2025).

The mytorus model parameters include the line flux normalization, the power-law index of the continuum (coupled to that of the "pow" component), the inclination of the emitting gas, a velocity shift parameter, and the column density of the emitting gas. Absent an inclination-sensitive convolution function, the inclination does not shape the line, and we fix an arbitrary value of 30°. We found no evidence of a velocity shift and fix a value of zero in all components for convenience. The data lack the sensitivity to place strong constraints on the gas column density, so we fix a value of $N_{\rm H} = 1.6 \times 10^{23}$ cm^{-2}, consistent with values measured in NGC 4151 (XRISM Collaboration et al. 2024). Each "mytorus" component is broadened with a Gaussian via the "vgau" function within SPEX, for which the Gaussian width σ is the only parameter. Each line component is therefore characterized by a flux normalization and width.

The best-fitting basic model parameters are shown in Table 1. The normalization of the "mytorus" components has a consistent order of magnitude of $\sim 10^{8}$ (in the same units as the power law), with a factor of $\sim$3 difference between the smallest and largest values. In contrast, the Gaussian widths show larger differences from one component to the next. At $\sigma = 370^{+150}_{-170}$, $\sigma = 2200^{+600}_{-500}$, and $\sigma = 20,000^{+6000}_{-4000}$ km s^{-1}, each component is separated by a 1 order of magnitude difference. The individual components as modeled are shown in Figure 2.

3.2. A Detailed Physical Model

To better understand the geometry of the accretion flow, we replace simple Gaussian broadening of the Fe K$_\alpha$ emission-line components with the SPEX function "spei." This function includes relativistic effects and is sensitive to the inclination of the emission region(s). Owing to the limited sensitivity of the data, we hold most parameters fixed at their default values and elect to fit for the inner emission radius and inclination of each component. Of the fixed values, the most important is the emissivity index ($J \propto r^{-q}$). We adopt a value of $q = 3$ as per a flat disk; in this case, the measured inclinations may better reflect the difference between the systemic inclination and the opening angle of the emission geometry relative to a planar disk (XRISM Collaboration et al. 2024).

We search for photoionized emission and absorption using the "pion" model. This model calculates the emission and absorption from a slab of gas, using the best-fit continuum at each step of the minimization process. The spectral energy distribution of AGN is dominated by UV or EUV emission; obtaining robust results from pion requires an accurate characterization of the spectral energy distribution (SED) over the 0.0136–13.6 keV band. We examined archival Hubble UV spectra of Mrk 279, but we were not able to derive a reliable continuum at the shortest, most critical wavelengths. Broadly following the procedure adopted in NGC 4151 (X. Xiang et al. 2025), we include a blackbody with a temperature of $kT = 0.017$ keV with a 10:1 flux ratio relative to the weaker power law. Both of these continuum components are then fed into "pion."

The pion absorption components are characterized by fitting for the gas column density ($N_{\rm H}$), ionization parameter ($\xi = L/nr^{2}$, where n is the gas number density and L is the ionizing luminosity), velocity broadening (σ_v), and bulk velocity shift (v_z). For simplicity, we assume a covering factor of 0.5 for all absorption components. Rather than random searches for winds, we conduct limited, directed searches for absorption from "warm absorbers" at very low shifts and flows with velocities close to $v \simeq 0.3c$ as per PDS 456 (XRISM Collaboration et al. 2025). In practice, the column density and geometric covering factor ($f_{\rm cov} = \Omega/4\pi$) of emission components are partly degenerate for photoionized emission. In searching for photoionized emission at low-velocity shifts, then, we fix an optically thin column density of $N_{\rm H} = 1 \times 10^{23}$ cm^{-2} and fit for the covering factor in a range of 0–1. The total best-fit physical model can be summarized as follows:

$$reds * hot * [(bb + pow * etau_{low} * etau_{hi} + MYT_1 * spei + MYT_2 * spei + MYT_3 * spei) * pion_1 * pion_2 * pion_3]. \quad (1)$$

Here, pion$_1$ and pion$_2$ model absorption, and pion$_3$ models emission. The Cash statistic of the best-fit physical model is $C = 693$ for $\nu = 664$ degrees of freedom (dof), well within the expected Cash statistic of 690 ± 37, indicating a good fit (J. S. Kaastra 2017). Table 2 presents the best-fit parameters for the physical model, as well as some derived properties for the absorption components, including launching radii, mass outflow rates, and kinetic powers. The fit in a broadband view is shown in Figure 3. Figure 4 depicts the breakdown of each emission and absorption component of the best-fit model. The best-fit model gives X-ray flux of $F_{2-10} = 2.1 \times 10^{-11}$ erg cm^{-2} s^{-1} in the 2–10 keV band and a total ionizing luminosity of $L_{\rm ion}^{\rm all} = 1.3 \times 10^{45}$ erg s^{-1}. Assuming $L_{\rm bol} = 2L_{\rm ion}^{\rm all}$, we estimate the bolometric luminosity of Mrk 279 to be approximately 2.6×10^{45} erg s^{-1}, yielding an Eddington ratio of $\lambda_{\rm Edd} = L_{\rm bol}/L_{\rm Edd} = 0.5$ with $L_{\rm Edd} \equiv 4\pi G M_{\rm BH} m_{\rm p} c/\sigma_{\rm T} \simeq 4.8 \times 10^{45}$ erg s^{-1}.

The significance of each Fe K$_\alpha$ emission-line component and each pion component is evaluated by removing it from the full model, refitting, and examining the difference in the fit

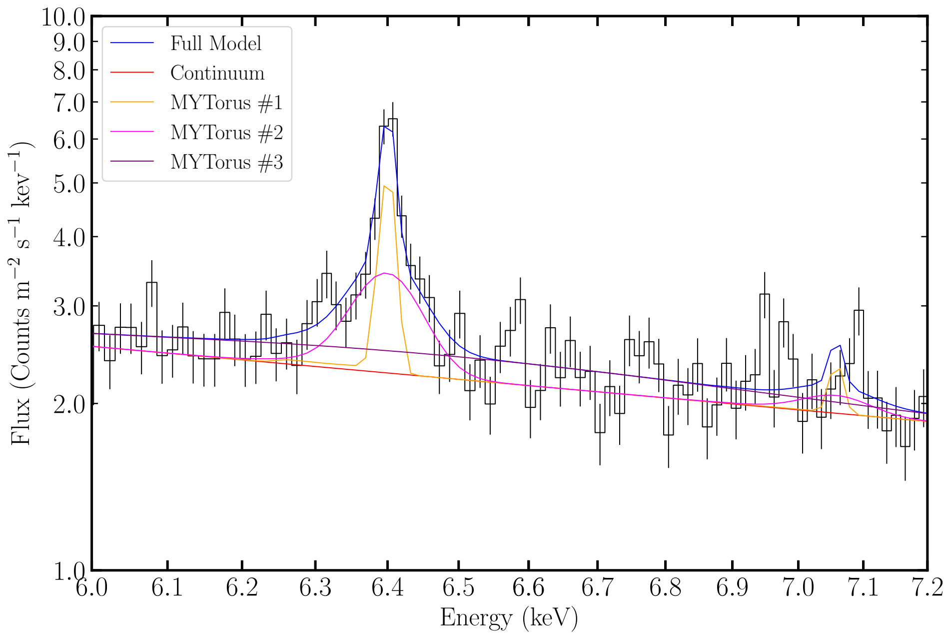

Figure 2. Simple model of Mrk 279 with Gaussian-broadened "mytorus" components. The full model is plotted in blue, while the continuum is shown in red. The individual "MYTorus" components are shown in orange, magenta, and purple. The data are plotted in the rest frame.

statistic. To assess the significance of each component, we compute the small sample Akaike information criterion (AIC; H. Akaike 1974; D. Emmanoulopoulos et al. 2016), defined as AIC $= 2p–2C_L + C + 2p(p + 1)/(n–p–1)$, where C is the C-stat of the fit, C_L is the C-stat of the best-fit model, $n = 687$ is the number of data bins, and $p = 23$ is the number of free parameters in the model. In Table 2, we report the change in AIC (ΔAIC). A value of $\Delta\text{AIC} < -10$ indicates that the component is strongly required to account for the spectral features, while $\Delta\text{AIC} < -2$ provides substantial evidence (K. P. Burnham & D. R. Anderson 2002). We also report a complementary detection significance (DS) in units of Gaussian-equivalent sigma, derived from the p-value associated with the changes in C-stat and the difference in dof.

3.2.1. Neutral Fe Kα Emission Components

The significance of each line component within the total model is listed in Table 2. The narrowest component is the most significant, followed by the intermediate-width component and the broadest component. The broadest component is clearly preferred by the model, as judged by the AIC, but is only significant at the 2.4σ level of confidence when only considering the p-value associated with changes in the Cash statistic. These tests measure the significance of adding a third component to a complex line profile. A full measure of the significance of each component might be better indicated by dividing the flux of each component by its 1σ minus-side error. This metric indicates that the components are significant at the 5σ, 4.3σ, and 3σ levels of confidence.

The narrow core of the Fe K_α line is found to originate at a radius of $r = 22000^{+231000}_{-11000}\ GM/c^2$. This is likely better viewed as a lower limit of $r \geqslant 10^4 GM/c^2$. These values are compatible with the inner wall of the molecular torus. The intermediate-width component is measured to originate at $r = 1560^{+5750}_{-1480}\ GM/c^2$. This range of radii is compatible with an inner X-ray extension to the optical BLR. The difference in implied radius between this component and the narrow core is consistent with dust reverberation studies that establish the inner wall of the torus is only a few times larger than the optical BLR (T. Minezaki et al. 2019). The broadest component of the emission line is found to have an inner radius of $r = 81^{+280}_{-75}\ GM/c^2$. It is important to note that this value includes the ISCO for a black hole with low spin but would also allow for a radially truncated disk.

The inclinations of all three components are statistically consistent but poorly constrained. The upper limits allow for inclinations exceeding 80°, which is implausible in an unobscured Seyfert-1 AGN. The large uncertainties on the inclination are a reflection of the lower flux and modest Fe K_α emission line observed from Mrk 279, and they are partly responsible for large uncertainties on the inner radius of each component.

3.2.2. Photoionized Emission and Absorption Components

The fits revealed one photoionized emission component (pion$_3$). The appearance of Fe XXVI emission (Lyα_1 and α_2 at 6.95 and 6.97 keV) and the absence of Fe XXV emission (close to 6.7 keV) leads to a very high ionization parameter, $\log \xi = 4.8 \pm 0.1$ (the ionization parameter ξ has units of erg cm s^{-1}). The covering factor hit the upper bound of 1.0, with a 1σ lower limit of 0.58; this signifies that the emitting gas may have a nearly spherical distribution. This component is nominally but not significantly redshifted, with a velocity of $v_z = 360^{+390}_{-370}$ km s^{-1}. Factoring in all of these properties, the emission may be a slow, wide-angle wind or failed wind. For this gas not to appear as a "warm absorber," its column density must be particularly low, or it must lie above the direct line of sight to the central engine. Its ionization is much higher than X-ray components that have been observed in the optical "narrow-line region" (see J. Wang et al. 2011). The line position is marked as gray dashed vertical lines in both Figures 3 and 4. The emission component is statistically required with $\Delta\text{AIC} = -8.3$ (DS $= 3.1\sigma$) and appears to

Table 2
The Detailed Physical Model Parameters

Parameters				
$C/\nu = 693/664$	`powerlaw`			
Γ	$1.67^{+0.01}_{-0.01}$	…	…	…
Norm (10^{52}ph s^{-1}keV^{-1})	$1.09^{+0.02}_{-0.02}$	…	…	…
		`MYT`$_1$	`MYT`$_2$	`MYT`$_3$
$r(GM/c^2)$	…	$21500^{+231000}_{-11000}$	1560^{+5750}_{-1480}	81^{+280}_{-75}
θ	…	27^{+60}_{-15}	34^{+53}_{-24}	33^{+53}_{-9}
Norm. (10^7)	…	10^{+3}_{-2}	13^{+3}_{-3}	6^{+2}_{-2}
$\Delta C/\Delta\nu$	…	$-19/-3$	$-16/-3$	$-10/-3$
ΔAIC (DS)	…	$-13(3.7\sigma)$	$-10(3.4\sigma)$	$-4(2.4\sigma)$
		`pion`$_1$	`pion`$_2$	`pion`$_3$
$N_{\rm H}$ (10^{24} cm^{-2})	…	$0.056^{+0.017}_{-0.020}$	$0.043^{+0.015}_{-0.011}$	0.1^{-}
$\log\xi$ (erg cm s^{-1})	…	$4.40^{+0.20}_{-0.32}$	$4.23^{+0.20}_{-0.18}$	$4.84^{+0.14}_{-0.12}$
σ_v (km s^{-1})	…	920^{+260}_{-590}	670^{+190}_{-240}	880^{+370}_{-260}
v_z (km s^{-1})	…	-66400^{+610}_{-270}	-99400^{+430}_{-170}	360^{+390}_{-370}
$f_{\rm cov}$	…	…	…	$1^{+0}_{-0.42}$
$\Delta C/\Delta\nu$	…	$-12/-4$	$-12/-4$	$-17/-4$
ΔAIC (DS)	…	$-3.3(2.4\sigma)$	$-3.5(2.4\sigma)$	$-8.3(3.1\sigma)$
r_1 (GM/c^2) Equation (4)	…	$1.6^{+0.5}_{-0.6}\times10^5$	$3.1^{+1.1}_{-0.8}\times10^5$	…
r_2 (GM/c^2) Equation (5)	…	$41^{+0.7}_{-0.3}$	$18^{+0.2}_{-0.1}$	…
$f_{\rm v_{min}} = r_2/r_1$	…	$2.5^{+1.5}_{-0.6}\times10^{-4}$	$0.6^{+0.2}_{-0.1}\times10^{-4}$	…
$\dot{M}_{\rm out}/f_{\rm v}$ ($M_\odot$/yr) Equation (2)	…	138^{+81}_{-72}	300^{+175}_{-101}	…
$\dot{E}_k/f_{\rm v}\times10^{46}$ (erg s^{-1}) Equation (3)	…	19^{+11}_{-10}	93^{+55}_{-32}	…
$\dot{E}_k/L_{\rm Edd}/f_{\rm v}$	…	40^{+23}_{-21}	195^{+110}_{-70}	…
$\dot{E}_k/L_{\rm Edd}/f_{\rm v}\times f_{\rm v_{min}}$	…	$1^{+0.6}_{-0.5}$(%)	$1^{+0.7}_{-0.4}$(%)	…
L_{ion}^{in} ($\times10^{45}$erg s^{-1})	…	$1.27^{+0.74}_{-0.66}$	$1.25^{+0.73}_{-0.42}$	…
$\dot{p}_{\rm rad}$ (dyn) Equation (7)	…	$5.4^{+3.1}_{-2.8}\times10^{34}$	$8.3^{+4.9}_{-2.8}\times10^{34}$	…
$\dot{p}_{\rm out}/f_{\rm v}$ (dyn) Equation (6)	…	$0.6^{+0.3}_{-0.3}\times10^{38}$	$1.9^{+1.1}_{-0.6}\times10^{38}$	…

Note. The upper panel (separated by the double horizontal lines) of this table presents best-fit parameters of the model, the change in C-stats/dof ($\Delta C/\Delta\nu$), the change in AIC (ΔAIC), and the detection significance (DS) for each component. The lower panel of this table provides the key wind parameters, including launching radius (r_1, r_2) and the lower limit of volume filling factor ($f_{\rm v_{min}}$). The values of mass outflow rate $\dot{M}_{\rm out}/f_{\rm v}$, kinetic power $\dot{E}_{\rm k}/f_{\rm v}$ assuming a unity volume filling factor, the ratio of kinetic power to the Eddington limit for both unity and minimum filling factors, the input ionizing luminosity $L_{\rm ion}^{\rm in}$, radiation momentum flux $\dot{P}_{\rm rad}$, and outflow momentum rate assuming unity filling factor $\dot{P}_{\rm out}/f_{\rm v}$ are presented as well. The best-fit model gives an X-ray flux of $F_{2-10} = 2.1\times10^{-11}$ erg cm^{-2} s^{-1} in the 2–10 keV band and a total ionizing luminosity of $L_{\rm ion}^{\rm all} = 1.3\times10^{45}$ erg s^{-1}. Assuming $L_{\rm bol} = 2L_{\rm ion}^{\rm all}$, we estimate the bolometric luminosity of Mrk 279 to be approximately 2.6×10^{45} erg s^{-1}, yielding an Eddington ratio of $\lambda_{\rm Edd} = L_{\rm bol}/L_{\rm Edd} = 0.5$.

confirm prior reports of Fe XXVI emission in Mrk 279 (e.g., E. Costantini et al. 2007, E. Costantini et al. 2010).

Two absorption components (pion$_1$ and pion$_2$) are tentatively detected, with blueshifted velocities of approximately $v_z \sim 6.6\times10^4$ and $v_z \sim 9.9\times10^4$ km s^{-1} or 0.22c and 0.33c (see Figures 3 and 4). These components represent only modest improvements to the fit, with ΔAIC $= -3.3$ and -3.5, respectively (roughly 2.4σ individually), and we regard them with some skepticism. The narrow widths of the lines in these zones ($\sigma = 920^{+260}_{-590}$ and $\sigma = 670^{+200}_{-240}$ km s^{-1}, respectively) would require clumping in order for the velocities to remain distinct through an acceleration phase. A brief exploration of the feedback properties of these tentative outflows is merited. In this examination, we broadly follow the procedure in X. Xiang et al. (2025).

The mass outflow rate can be written as

$$\dot{M}_{\rm out} = 4\pi f_{\rm cov}\,\mu m_p \frac{L_{\rm ion}^{\rm in}}{\xi} v_{\rm out} f_{\rm v}\,, \tag{2}$$

where $\mu = 1.23$ is the mean atomic weight, m_p is the proton mass, $f_{\rm cov}$ and $f_{\rm v}$ are angular and volume filling factors, and we have used the ionization parameter formalism to replace r^2 with $L_{\rm ion}/\xi$. Within SPEX, the ionizing luminosity incident on each absorber $L_{\rm ion}^{\rm in}$ is determined directly from the outputs parameter "lixi" of "pion" component, defined as $L_{\rm ion}^{\rm in}/\xi$.

Assuming a unity filling factor $f_{\rm v} = 1$ (the upper limit), the mass outflow rates for the two absorbers are $\dot{M} = 138^{+81}_{-72}$ and $\dot{M} = 300^{+175}_{-101}\,M_\odot$ yr^{-1}. These rates far exceed the Eddington mass accretion rate $\dot{M}_{\rm Edd} \equiv L_{\rm Edd}/\eta c^2 = 0.8\,(M_\odot/{\rm yr})$ for a radiative accretion efficiency of $\eta = 0.1$.

The kinetic power of a wind, assuming it reaches a terminal velocity without significant acceleration, is given by

$$\dot{E}_k = \frac{1}{2}\dot{M}_{\rm out} v_{\rm out}^2. \tag{3}$$

For a unity volume filling factor, the two ultrafast outflows (UFOs) have kinetic power of $L_{\rm kin} = 19^{+11}_{-10}\times10^{46}$ and $L_{\rm kin} = 93^{+55}_{-32}\times10^{46}$ erg s^{-1}. These values are approximately 40× and 200× more than the radiative Eddington luminosity of Mrk 279.

The launching radius of the wind can be constrained using two complementary estimates that provide upper and lower

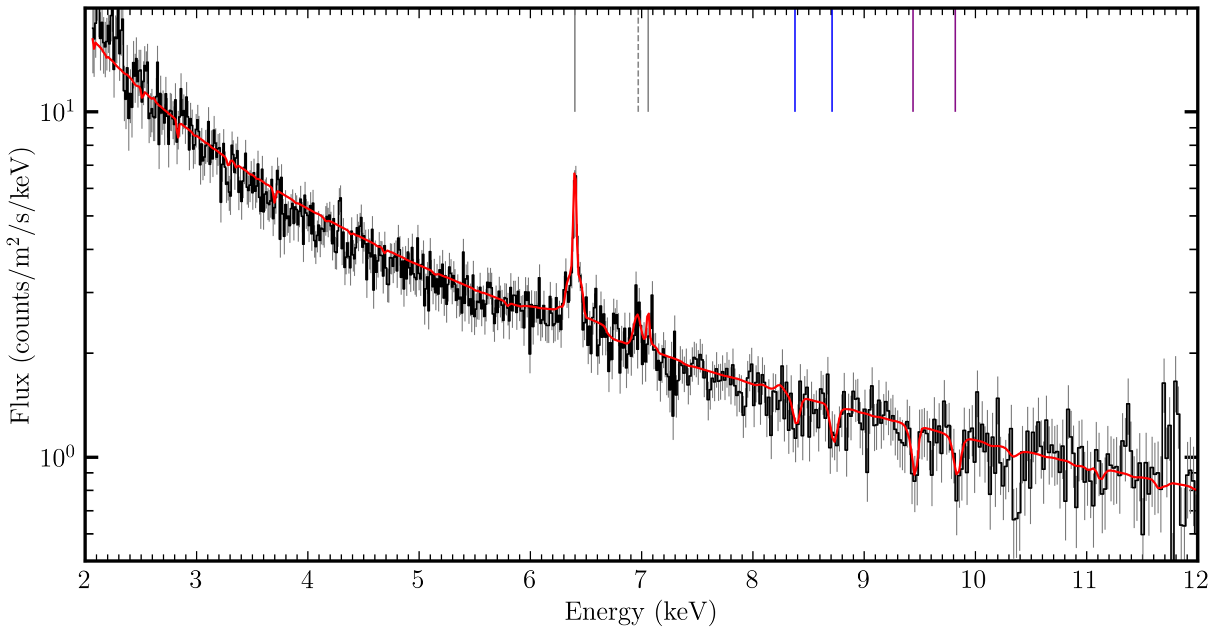

Figure 3. The time-averaged XRISM/Resolve spectrum of Mrk 279. The data are plotted in the rest frame and binned using the "optimal" algorithm for fitting and by a further factor of 4.0. The model shown in red is the best-fit extended physical model, including three components for the neutral Fe K emission lines, photoionized emission contributing an H-like Fe XXVI line at 6.97 keV, and photoionized absorption from tentative fast wind components. The solid gray lines indicate the lab energies of the neutral Fe K$_\alpha$ and Fe K$_\beta$ lines. The dashed gray line indicates the lab energy for the Fe XXVI emission line. The blue and purple lines indicate He-like Fe XXV and H-like Fe XXVI line pairs from potential UFOs at $v \simeq 0.22c$ and $v \simeq 0.33c$. Please see the text and Table 2.

limits, assuming that the gas originates in a thin shell ($\Delta r/r \ll 1$). Assuming the radial thickness of the absorber (Δr) does not exceed its distance from the source, and using the relation $N_{\rm H} = n\Delta r \leqslant f_{\rm v} nr$, the upper limit becomes

$$r_{\rm max} = \frac{L_{\rm ion} f_{\rm v}}{\xi N_{\rm H}} = r_1 f_{\rm v}, \quad (4)$$

where $f_{\rm v}$ is the volume filling factor and $r_1 = L_{\rm ion}/\xi N_{\rm H}$ is the so-called "absorption radius," which can be computed directly from the measured values of $N_{\rm H}$ and ξ. This absorption radius provides a useful upper bound on the launching radius.

On the other hand, assuming that the observed outflow velocity is comparable to the local escape velocity, we can estimate a lower limit for the launching radius as follows:

$$\begin{aligned} r_{\rm min} &= \frac{2GM}{v_{\rm out}^2} = \frac{2GM}{v_{\rm z}^2}\cos^2\theta \\ &= r_2 \cos^2\theta, \end{aligned} \quad (5)$$

where $r_2 = 2GM/v_{\rm z}^2$ is referred to as the "wind radius," $v_{\rm z}$ is the line-of-sight velocity, and θ is the inclination of the flow relative to the line of sight. For small inclination angles ($\cos\theta \approx 1$), the ratio r_2/r_1 provides an estimate of the minimum volume filling factor, with the constraint that $r_{\rm max} \geqslant r_{\rm min}$.

The inferred "absorber radii" for the two absorption components are $1.6^{+0.5}_{-0.6} \times 10^5$ and $3.1^{+1.1}_{-0.8} \times 10^5$, and the "wind radius" values are $41^{+0.7}_{-0.3}$ and $18^{+0.2}_{-0.1}$, in units of GM/c^2. The overlapping ranges of their inferred radii suggest that the two components may have a common origin. The lower limits for the volume filling factors are $2.5^{+1.5}_{-0.6} \times 10^{-4}$ and $0.6^{+0.2}_{-0.1} \times 10^{-4}$. If these values are correct, the mass outflow rates would be comparable to the inferred accretion rates, and the putative UFOs in Mrk 279 would plausibly fall below the $L_{\rm kin} \geqslant 0.5\%–5\% L_{\rm Edd}$ threshold for galaxy altering feedback (T. Di Matteo et al. 2005; P. F. Hopkins & M. Elvis 2010).

To further investigate the energetics and possible driving mechanisms, we calculate the outflow momentum rate,

$$\dot{p}_{\rm out} = \dot{M}_{\rm out} v_{\rm out}, \quad (6)$$

and the radiation momentum flux,

$$\dot{p}_{\rm rad} = \frac{L_{\rm bol}^{\rm in}}{c}, \quad (7)$$

where $L_{\rm bol}^{\rm in}$ is the corrected bolometric luminosity incident on each absorber assuming $L_{\rm bol}^{\rm in} = 2L_{\rm ion}^{\rm in}$.

Assuming a unity volume filling factor, the two outflow components carry momentum fluxes of $\dot{p}_{\rm out} \sim 10^{37-38}$ dyn, exceeding by 3–4 orders of magnitude their corresponding radiation momentum fluxes ($\dot{p}_{\rm rad} \sim 10^{34-35}$ dyn). Under these conditions, radiation pressure alone is insufficient to accelerate these outflows. Radiation pressure on lines alone is likely ruled out by the high ionization of the putative UFO components, which leaves no UV transitions and provides no force multiplier. In this scenario, it is not clear that even magnetic pressure could drive the flows.

If, however, the absorbing gas is highly clumpy, where the effective filling factor could be as low as $\sim 10^{-4}$, the outflow momentum rate drops to only 30% of the radiation momentum flux. In this case, radiation pressure in the form of electron scattering pressure could dominate. In scenarios where electron scattering pressure plays an important role, a direct proportionality between $\dot{p}_{\rm out}$ and $\dot{p}_{\rm rad}$ is expected (J. Gofford et al. 2015). The fact that pion$_2$, which has the larger outflow momentum, also exhibits the larger radiation momentum flux is consistent with this picture.

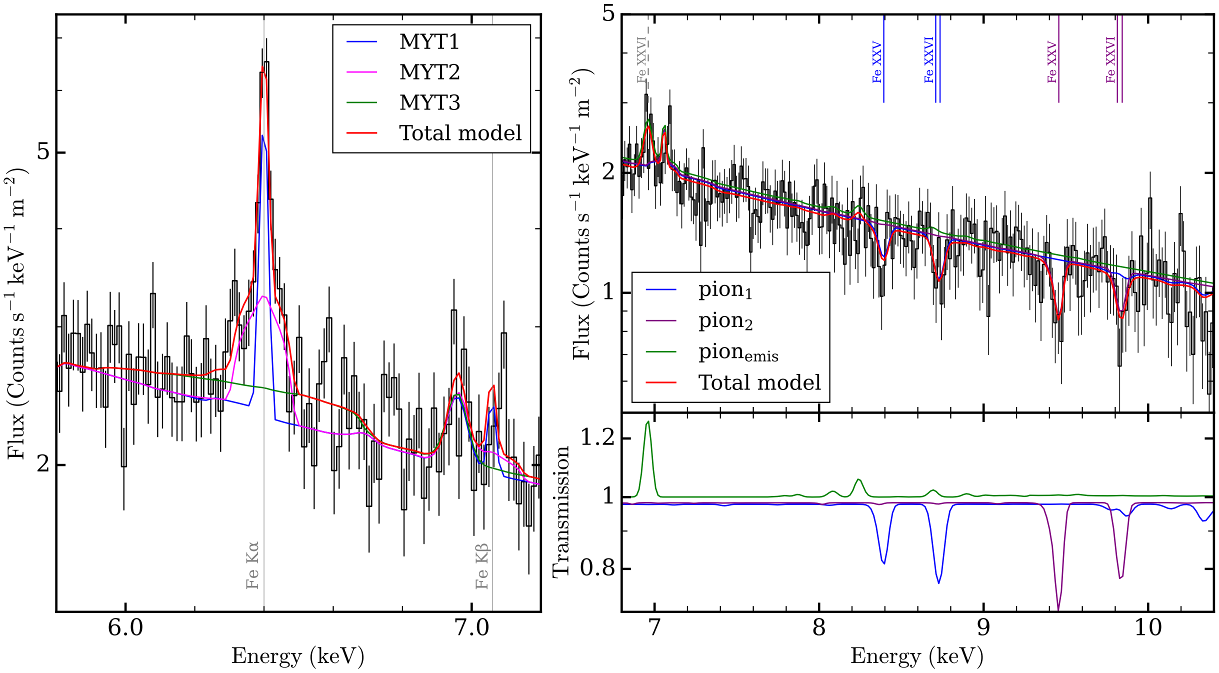

Figure 4. The zoomed-in spectrum and the best-fit extended physical model (red), including the breakdown of the components for Fe K emission lines and photoionized emission/absorption lines. The data are plotted in the rest frame.

4. Discussion

We analyzed the first XRISM/Resolve spectrum of Mrk 279, a nearby Seyfert-1 AGN with a history of compelling properties, including a complex and variable Fe K_α emission-line profile. Adopting a set of models similar to those applied to the XRISM spectra of NGC 4151, we find that the line complex contains components that can be linked to the inner face of the torus, an inner extension of the optical BLR, and the inner accretion disk. In this sense, our observation confirms that even narrow Fe K_α lines represent incisive probes of the central engine in Seyfert galaxies. Similar to prior studies, the Resolve spectrum does not require slow, ionized, "warm absorber" winds in the Fe K band. The data reveal tentative indications of a very fast wind with at least superficial similarities to the UFOs that XRISM has revealed in NGC 4151 and especially PDS 456 (X. Xiang et al. 2025, XRISM Collaboration et al. 2025). In this section, we place the geometric constraints obtained from Mrk 279 into the broader context of recent XRISM results, critically examine the putative fast outflows and how they might be drive, and suggest directions for future studies of Mrk 279.

4.1. Fe K Lines and Accretion Flow Geometries

XRISM observations of NGC 4151 established that the components of the Fe K_α emission complex may trace all of the key geometries within the central engine (XRISM Collaboration et al. 2024). Our observation of Mrk 279 appears to confirm this and signals that similar insights can be gained even from AGN with lower fluxes. The net exposure of 168 ks required 300 ks or 3.5 days to accumulate, owing to the modest efficiency of the low-Earth orbit. This is much shorter than the Hβ reverberation lag timescale of $\tau = 18 \pm 1$ days (Y. Zu et al. 2011). Our single XRISM observation does not permit the detection of a clear line response to time variations in the central engine.

The common features of the spectra in Mrk 279 and NGC 4151 are at least qualitatively consistent with a picture wherein the intermediate component the narrow Fe K line traces an inner, low-velocity region of the BLR close to the disk. If the BLR represents an outflow, the gas must be detected before acceleration occurs downstream. This may offer qualitative support for models that rely on dust—onto which iron may accumulate—to launch the winds that we identify as the BLR (B. Czerny et al. 2015). If the putative UFOs are confirmed in later work (see below), the broadest emission component could plausibly be associated with emission from the wind, similar to the case of PDS 456 (XRISM Collaboration et al. 2025).

The efficacy with which X-rays reveal the geometry of the central engine should also be assessed by looking at a broad range of sources and examining potential trends with parameters like the Eddington fraction. We therefore collected radius constraints from the recent literature on XRISM observations of AGN. Similar to our analysis, fits with Speith-broadened "mytorus" components have been reported from NGC 4151, Cen A, and M81* (XRISM Collaboration et al. 2024, D. Bogensberger et al. 2025, J. M. Miller et al. 2025). To these, we added the corresponding results from a forthcoming work on the first XRISM/Resolve spectrum of the Seyfert-1 galaxy NGC 3783 (C. Li et al. 2025).

Figure 5 plots the approximate Eddington fraction of each source versus the inner radius of the components measured in Resolve spectra. (If the Eddington fraction drives the nature of the accretion flow, it is really the independent variable, but the plot depicts radius on the horizontal axis because this preserves notional contact with cartoons for how different geometries are laid out with radius.) Although the uncertainties on the components in Mrk 279 are larger than for NGC 4151, it is clear that the inferred radii are in formal agreement. Here, it is again worth noting that some of the inclinations are poorly constrained and that the results depend on the assumed emissivity profile, but in this comparison the same emissivity

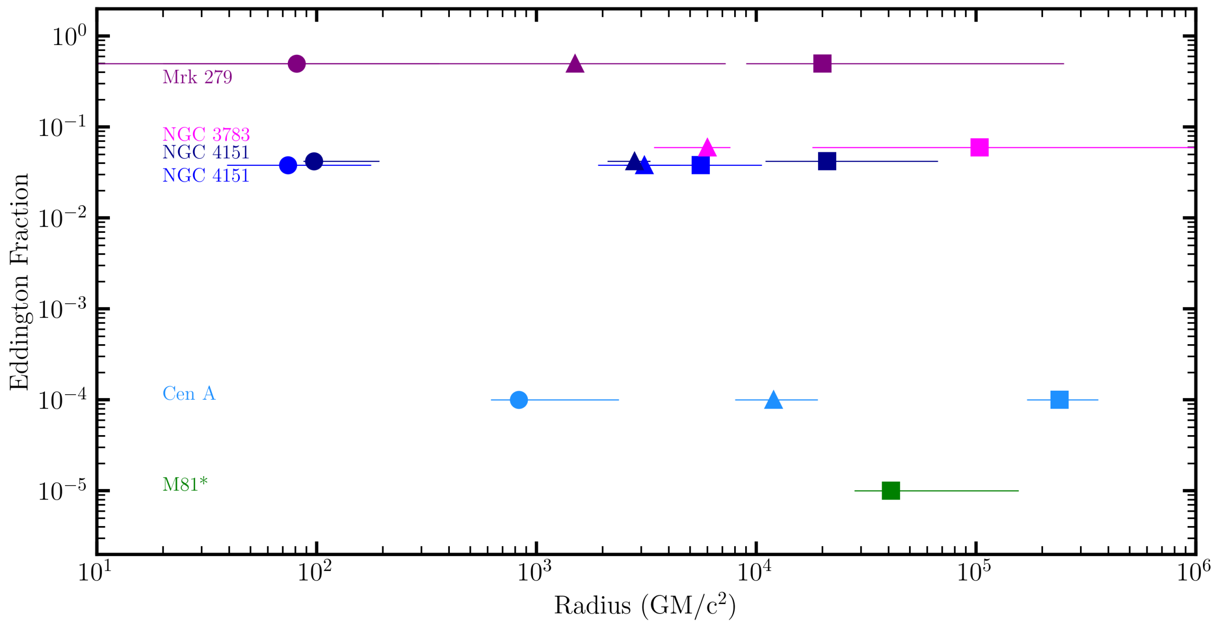

Figure 5. A comparison of the inner radii measured for Fe K_α line components in a subset of XRISM spectra of local AGN. All of the radii are based on blurred "mytorus" modeling of Resolve spectra; please see the text for details. With several important caveats, this plot suggests that Resolve data are able to separate line emission from the inner disk, BLR, and torus and capable of tracing trends with Eddington fraction.

is assumed for all sources. The line complex in NGC 3783 includes a very broad-line component from the innermost disk, potentially as close as $2GM/c^2$ (C. Li et al. 2025). The line in M81* does not statistically require multiple components; its single component width is consistent with the torus values inferred in NGC 4151 and Mrk 279.

The inclination of the optical BLR in Mrk 279 is constrained to be $\theta = 29.^\circ1 \pm 3.^\circ4$ with respect to our line of sight (P. R. Williams et al. 2018). This is consistent with the value that we have measured from the intermediate-width component of the Fe K_α line, $\theta = 34^{+53}_{-24}$ degrees, although our uncertainties do not provide a strong constraint. In some AGN, the broad accretion flow geometry may be consistent with a "bowl" geometry (e.g., Gravity Collaboration et al. 2024); in NGC 4151, the observation of progressively lower effective inclinations with radius may indicate such a geometry (XRISM Collaboration et al. 2024). Deeper XRISM observations of Mrk 279 that achieve tighter inclination constraints will be able to test this.

Our three-component model for the Fe K emission lines may not capture all of the information in the Mrk 279 spectrum, or it may fail to interpret all of the information correctly:

First, the Fe K_α line complex may have an intriguing degree of complexity on its red wing (see Figure 2). In the time-averaged and flux-selected spectra, there is evidence of narrow emission at 6.32 keV. This putative feature is inconsistent with the edge expected at 6.25 keV–150 eV losses in 180° Compton scattering. We find that it can be modeled in terms of a very narrow ring of emission, only tens of radii from the black hole. Qualitatively, this may be consistent with numerical simulations of warped and torn disks in accretion disks that are misaligned with the black hole spin vector (e.g., C. Nixon et al. 2012). However, this is an extreme interpretation, and deeper observations are required to test it.

Second, our model may be deficient in assuming that all of the K_α and K_β flux is due to neutral Fe. The predicted K_β line is only just consistent with the 1σ errors on the data (see Figures 1 and 2). Moreover, at only a slightly higher energy, just shy of 7.1 keV, a bin stands above the continuum. This may signal a contribution from slightly ionized iron. In this case, the blue wing of the K_α complex would also have to correspond to ionized iron, rather than just velocity broadening of a neutral line. The data disfavor this interpretation because a good fit to the the K_β line would require a K_α line that is stronger than the data. It is possible that the appearance of the Fe K_β line is impacted by a $v \simeq 4000\,\mathrm{km\,s^{-1}}$ wind that covers or distorts this emission with Fe XXVI absorption.

We also note that a small upturn in the data below 3 keV causes our model to underestimate the data there and to slightly overestimate the data in the 3–4 keV band. This disparity is likely the result of our use of the large or "L" format response matrix, rather than the extralarge of an "XL" matrix. This was merely an expedient choice because fits and error scans with complex convolution functions and layered photoionization models are extremely difficult with "XL" matrices. We conducted additional fits with a broken power law to understand the influence of the artificial upturn at low energy; the fit through the Fe K band and above is unaffected.

4.2. The Search for UFOs

Our targeted search for UFOs in Mrk 279 was motivated by its relatively high Eddington fraction and the dramatic XRISM spectra obtained from PDS 456 (XRISM Collaboration et al. 2025). In that source, the narrow nature of the observed lines nominally points to confined clumps of gas. If the same arguments regarding volume filling factors and clump sizes apply in Mrk 279, the fast winds would transfer hundreds of solar masses of material per year and enormous kinetic energy, easily meeting the theoretical threshold for galaxy shaping feedback (T. Di Matteo et al. 2005; P. F. Hopkins & M. Elvis 2010). However, unlike PDS 456, there is no obvious flaring in the light curve of Mrk 279 to enable constraints on distances, size scales, and filling factors. It is possible that the putative UFOs in Mrk 279—if real—have a much lower volume filling factor and therefore convey orders-of-magnitude lower mass flux and kinetic power. This may be more plausible given that the kinetic power of a true PDS 456-like wind would exceed the radiative Eddington limit in Mrk 279 by 2 orders of magnitude.

Deeper XRISM observations of Mrk 279—for instance, with the gate valve in the "open position"—will be able to test these weak indications for UFOs. In this configuration, H-like lines from low-Z elements that are predicted by the "pion" models in Table 2 will be within the passband and should be resolved and detected. It may also be possible to target future observations of Mrk 279 to observe a particularly bright X-ray phase, an interval wherein the emission is soft and less likely to fully ionize the same fraction of the gas in our line of sight, or other favorable circumstances. A promising approach might be to use variability in the absorption features to infer the gas density; this would demand a series of coordinated, timed observations.

The Resolve spectrum of Mrk 279 does not require a "soft excess" component owing to its limited passband. However, prior XMM-Newton observations require such a component at low energy (E. Costantini et al. 2010). For plausible characterizations of the soft excess in terms of a steeper power law or cool thermal component and plausible flux levels, we find that including this component in the SED only affects column densities and ionization parameters at the few percent level. Velocity widths and shifts are unaffected. The nature of the soft excess could also be investigated in an observation with the gate valve in an open position.

It is worth remarking that both Mrk 279 and PDS 456 lack evidence of slow-moving, highly ionized "warm absorber" winds in the Fe K band. In contrast, spectra of NGC 4151 reveal a rich diversity of wind speeds, including these extremes. It is tempting to speculate, then, that the most ionized warm absorbers may be suppressed at high Eddington fractions. Narrow-line Seyfert-1 AGN are thought to harbor relatively low-mass black holes accreting at high Eddington fractions; of these, NGC 4051 is the most proximal and brightest case. Even in the deepest Chandra gratings spectra of this source, there is little evidence for slow winds evident in the Fe K band (A. Ogorzalek et al. 2022). If future XRISM observations of a broader array of AGN confirm this, it may indicate that faster, wider-angle UFOs launched at higher Eddington fractions act to sweep away gas that was previously seen as highly ionized warm absorbers.

Acknowledgments

We thank the anonymous referee for insights that improved this manuscript. J.M.M. acknowledges helpful conversations with Liyi Gu and Jelle Kaastra.

Software: astropy (Astropy Collaboration et al. 2013, 2018, 2022), SPEX (v3.08.01, J. S. Kaastra et al. 2024), Matplotlib (J. D. Hunter 2007), NumPy (C. R. Harris et al. 2020), pandas (W. McKinney 2010; The pandas development team 2024).

ORCID iDs

Jon M. Miller https://orcid.org/0000-0003-2869-7682
Xin Xiang https://orcid.org/0000-0002-7129-4654
Doyee Byun (변도의) https:/orcid.org/0000-0002-3687-6552
Ehud Behar https://orcid.org/0000-0001-9735-4873
Laura Brenneman https://orcid.org/0000-0003-2663-1954
Edward Cackett https://orcid.org/0000-0002-8294-9281
Elisa Costantini https://orcid.org/0000-0001-8470-749X
Luigi Gallo https://orcid.org/0009-0006-4968-7108
Keith Horne https://orcid.org/0000-0003-1728-0304
Elias Kammoun https://orcid.org/0000-0002-0273-218X
Chen Li https://orcid.org/0000-0001-5493-7585
Abderahmen Zoghbi https://orcid.org/0000-0002-0572-9613

References

Akaike, H. 1974, ITAC, 19, 716
Astropy Collaboration, Price-Whelan, A. M., Lim, P. L., et al. 2022, ApJ, 935, 167
Astropy Collaboration, Price-Whelan, A. M., Sipőcz, B. M., et al. 2018, AJ, 156, 123
Astropy Collaboration, Robitaille, T. P., Tollerud, E. J., et al. 2013, A&A, 558, A33
Bentz, M. C., & Katz, S. 2015, PASP, 127, 67
Bogensberger, D., Nakatani, Y., Yaqoob, T., et al. 2025, PASJ, 77, S209
Burnham, K. P., & Anderson, D. R. 2002, Information and Likelihood Theory: A Basis for Model Selection and Inference (New York: Springer), 49
Cash, W. 1979, ApJ, 228, 939
Costantini, E., Kaastra, J. S., Arav, N., et al. 2007, A&A, 461, 121
Costantini, E., Kaastra, J. S., Korista, K., et al. 2010, A&A, 512, A25
Czerny, B., Modzelewska, J., Petrogalli, F., et al. 2015, AdSpR, 55, 1806
Di Matteo, T., Springel, V., & Hernquist, L. 2005, Natur, 433, 604
Emmanoulopoulos, D., Papadakis, I. E., Epitropakis, A., et al. 2016, MNRAS, 461, 1642
Event Horizon Telescope Collaboration, Akiyama, K., Alberdi, A., et al. 2019, ApJL, 875, L1
Gallo, L. C., Miller, J. M., & Costantini, E. 2023, arXiv:2302.10930
Gofford, J., Reeves, J. N., McLaughlin, D. E., et al. 2015, MNRAS, 451, 4169
Gravity Collaboration, Amorim, A., Bourdarot, G., et al. 2024, A&A, 690, A76
Harris, C. R., Millman, K. J., van der Walt, S. J., et al. 2020, Natur, 585, 357
Hayashida, K., Tomida, H., Mori, K., et al. 2018, Proc. SPIE, 10699, 1069923
Hopkins, P. F., & Elvis, M. 2010, MNRAS, 401, 7
Hunter, J. D. 2007, CSE, 9, 90
Ishisaki, Y., Kelley, R. L., Awaki, H., et al. 2022, Proc. SPIE, 12181, 121811S
Kaastra, J. S. 2017, A&A, 605, A51
Kaastra, J. S., & Bleeker, J. A. M. 2016, A&A, 587, A151
Kaastra, J. S., Mewe, R., & Nieuwenhuijzen, H. 1996, in 11th Colloquium on UV and X-ray Spectroscopy of Astrophysical and Laboratory Plasmas, ed. K. Yamashita & T. Watanabe, 411
Kaastra, J. S., Raassen, A. J. J., de Plaa, J., & Gu, L. 2024, SPEX X-ray spectral fitting package, v3.08.01, Zenodo, doi:10.5281/zenodo.12771915
Li, C., Kaastra, J. S., Gu, L., et al. 2025, A&A, submitted
McKinney, W. 2010, in Proc. of the 9th Python in Science Conf., ed. S. van der Walt & J. Millman, 56
Mehdipour, M., Kaastra, J. S., Eckart, M. E., et al. 2025, A&A, 699, A228
Miller, J. M., Behar, E., Awaki, H., et al. 2025, ApJL, 985, L41
Minezaki, T., Yoshii, Y., Kobayashi, Y., et al. 2019, ApJ, 886, 150
Murphy, K. D., & Yaqoob, T. 2009, MNRAS, 397, 1549
Nixon, C., King, A., Price, D., & Frank, J. 2012, ApJL, 757, L24
Ogorzalek, A., King, A. L., Allen, S. W., Raymond, J. C., & Wilkins, D. R. 2022, MNRAS, 516, 5027
Strauss, M. A., & Huchra, J. 1988, AJ, 95, 1602
Tashiro, M., Maejima, H., Toda, K., et al. 2021, Proc. SPIE, 11444, 1144422
The pandas development team 2024, pandas-dev/pandas: Pandas, v2.2.3, Zenodo, doi:10.5281/zenodo.13819579
Vasudevan, R. V., & Fabian, A. C. 2007, MNRAS, 381, 1235
Wang, J., Fabbiano, G., Elvis, M., et al. 2011, ApJ, 742, 23
Williams, P. R., Pancoast, A., Treu, T., et al. 2018, ApJ, 866, 75
Xiang, X., Miller, J. M., Behar, E., et al. 2025, ApJL, 988, L54
XRISM Collaboration, Audard, M., Awaki, H., et al. 2024, ApJL, 973, L25
XRISM Collaboration, Audard, M., Awaki, H., et al. 2025, Natur, 641, 1132
Zu, Y., Kochanek, C. S., & Peterson, B. M. 2011, ApJ, 735, 80